Opto-Electronic Advances

CN 51–1781/TN ISSN 2096–4579 (Print) ISSN 2097–3993 (Online)

Observation of polaronic state assisted sub-bandgap saturable absorption

Li Zhou, Yiduo Wang, Jianlong Kang, Xin Li, Quan Long, Xianming Zhong, Zhihui Chen, Chuanjia Tong, Keqiang Chen, Zi-Lan Deng, Zhengwei Zhang, Chuan-Cun Shu, Yongbo Yuan, Xiang Ni, Si Xiao, Xiangping Li, Yingwei Wang and Jun He

Citation: Zhou L, Wang YD, Kang JL, et al. Observation of polaronic state assisted sub-bandgap saturable absorption. *Opto-Electron Adv* **8**, 240312(2025).

https://doi.org/10.29026/oea.2025.240312

Received: 23 December 2024; Accepted: 7 April 2025; Published online: 21 May 2025

Related articles

2D Nb_2CT_x MXene/MoS_2 heterostructure construction for nonlinear optical absorption modulation

Yiduo Wang, Yingwei Wang, Yulan Dong, Li Zhou, Jianlong Kang, Ning Wang, Yejun Li, Xiaoming Yuan, Zhengwei Zhang, Han Huang, Mengqiu Long, Si Xiao, Jun He

Opto-Electronic Advances 2023 **6**, 220162 doi: 10.29026/oea.2023.220162

Polariton lasing in Mie-resonant perovskite nanocavity

Mikhail A. Masharin, Daria Khmelevskaia, Valeriy I. Kondratiev, Daria I. Markina, Anton D. Utyushev, Dmitriy M. Dolgintsev, Alexey D. Dmitriev, Vanik A. Shahnazaryan, Anatoly P. Pushkarev, Furkan Isik, Ivan V. Iorsh, Ivan A. Shelykh, Hilmi V. Demir, Anton K. Samusev, Sergey V. Makarov

Opto-Electronic Advances 2024 **7**, 230148 doi: 10.29026/oea.2024.230148

More related article in Opto-Electronic Journals Group website

OEA Opto-Electronic Advances

http://www.oejournal.org/oea

OE_Journal

@OptoElectronAdv

Opto-Electronic Advances

Article

June 2025, Vol. 8, No. 6

DOI: 10.29026/oea.2025.240312 CSTR: 32247.14.oea.2025.240312

Observation of polaronic state assisted sub-bandgap saturable absorption

Li Zhou[1], Yiduo Wang[1,2], Jianlong Kang[1], Xin Li[1], Quan Long[1], Xianming Zhong[1], Zhihui Chen[1], Chuanjia Tong[1], Keqiang Chen[3], Zi-Lan Deng[4], Zhengwei Zhang[1], Chuan-Cun Shu[1], Yongbo Yuan[1], Xiang Ni[1], Si Xiao[1], Xiangping Li[4], Yingwei Wang[1*] and Jun He[1*]

In soft-lattice lead-halide perovskites, the polaronic effects involving stabilization of localized charge character by structural deformations and polarizations have an important effect on the properties of functional materials such as the band gap, which has attracted considerable investigations. However, the concept of polaron assisted nonlinear photonics remains largely unexplored, which has a wide range of applications from optoelectronics to telecommunications and quantum technologies. Here, we report the first observation of the polaronic state assisted saturable absorption through sub-bandgap excitation with a redshift exceeding 60 meV. By combining photoluminescence, transient absorption measurements and density functional theory calculations, we explicate that the anomalous nonlinear saturable absorption under sub-bandgap excitation is caused by the transient picosecond timescale polaronic state formed by strong carrier/exciton-phonon coupling effect. The bandgap fluctuation caused by polaron formation can be further tuned through exciton-phonon coupling of perovskites with different Young's modulus. This suggests that we can design targeted soft lattice lead-halide perovskite with a specific structure to effectively manipulate exciton-phonon coupling and exciton-polaron formation. These findings profoundly expand our understanding of exciton-polaronic nonlinear optics physics and provide an ideal platform for developing actively tunable nonlinear photonics applications.

Keywords: polaron; perovskite; soft lattice; nonlinear optics; saturable absorption

Zhou L, Wang YD, Kang JL et al. Observation of polaronic state assisted sub-bandgap saturable absorption. *Opto-Electron Adv* **8**, 240312 (2025).

Introduction

Nonlinear optics, describing how light-matter interaction depends upon the intensity of light filed in a nonlinear manner[1], has offered an unparalleled approach for quantum material and information[2,3], all optical elements[4], integrated photonic devices[5–7], or biophotonics[8–10]. Nonlinear saturable absorption (SA) response as a typical nonparametric third-order nonlinear optical process (see details in Supplementary information Section 1) has led to various promising applications in ultrashort

[1]Hunan Key Laboratory of Nanophotonics and Devices, School of Physics, Central South University, Changsha 410083, China; [2]Beijing National Laboratory for Condensed Matter Physics, Institute of Physics, Chinese Academy of Sciences, Beijing 100190, China; [3]Faculty of Materials Science and Chemistry, China University of Geosciences, Wuhan 430074, China; [4]Guangdong Provincial Key Laboratory of Optical Fiber Sensing and Communications, Institute of Photonics Technology, College of Physics & Optoelectronic Engineering, Jinan University, Guangzhou 510632, China.

*Correspondence: YW Wang, E-mail: wyw1988@csu.edu.cn; J He, E-mail: junhe@csu.edu.cn

Received: 23 December 2024; Accepted: 7 April 2025; Published online: 21 May 2025

Open Access This article is licensed under a Creative Commons Attribution 4.0 International License.
To view a copy of this license, visit http://creativecommons.org/licenses/by/4.0/.

© The Author(s) 2025. Published by Institute of Optics and Electronics, Chinese Academy of Sciences.

pulse generation[11,12], and optical diodes[13]. This has sparked a research boom in the nonlinear optical response of two-dimensional materials[14,15]. In addition, the compelling demands for superior optical nonlinearity and active controlling nonlinear optical response of two-dimensional materials have further motivated intense research on exploring nonlinear optical modulation strategy including electric field regulation[16], excitation resonance[17] and heterojunction construction[18] etc. Substantial efforts have been devoted toward investigating polarons in two-dimensional material systems[19], with the aim of harnessing their potential as a solid-state medium for achieving enhanced nonlinear optical response[20,21].

Polarons, as quasiparticles arising from strong interaction between electrons and lattice vibrations of material, have enabled versatile control of materials' functionalities. Nontrivial polarization in exciton-polarons was induced by strong coupling of long-lifetime photoexcited carrier/exciton with local lattice distortions in material[22,23]. Compared with traditional semiconductors, the soft and polar lattice of lead halide perovskites (LHPs) usually exhibit large anharmonicity and dynamic disorder, leading to strong electron-phonon coupling[24,25]. The polarons model proposed in perovskites has impelled widespread research interests ranging from polaron formation photophysical mechanism[22,26], polarons dispersion relation detection[27,28], to polarons contributed optoelectronic applications (solar cells[29,30], laser[31], and photodetectors[32]). Efforts to understand exciton-polaron physics in soft lattice LHPs revealed that exciton polaronic feature enable enhanced sub-bandgap linear optical absorption and emission[33,34]. Very recently, polaronic states leading to giant anti-Stokes shift up to 220 meV have been achieved in two-dimensional perovskite systems[35], demonstrating the importance of exciton–phonon coupling in tailoring interplay between soft-lattice dynamics and optoelectronic properties in perovskite material systems. However, a direct signature of the correlation between polaronic states and nonlinear optical responses in LHPs has yet to be reported. Achieving this observation is crucial for revealing how exciton-phonon coupling influences nonlinear nanophotonic responses, which holds significant implications for optoelectronics and quantum technologies.

In this article, we demonstrate polaronic state assisted nonlinear saturable absorption (PSA_SA) response in perovskites by observing nonlinear optical bleaching under sub-bandgap excitation at room temperature. Our systematic multi-wavelength Z-scan measurements show that the PSA_SA can be observed in $CsPbBr_3$ under sub-bandgap excitation with redshifts up to 60 meV. Our robust photoluminescence (PL) and transient absorption (TA) spectroscopy studies unequivocally confirm that this anomalous SA is caused by the polaronic state formed by strong carrier/exciton-phonon coupling effect, that manifests by phonon-assisted up-conversion photoluminescence (UCPL) and prolonged rise time for the exciton band bleach in TA measurements. By employing density functional theory (DFT) calculations, we reveal the band edge energy fluctuations (~49 meV) attributed to lattice deformation in soft lattice $CsPbBr_3$, which provides additional evidence for understanding the mechanism of sub-bandgap photons absorption. We further demonstrate that the softer perovskite with smaller Young's modulus exhibits a larger band energy fluctuation (~125 meV), signifying that the polaronic state involved optical nonlinearity can be tailored through modification of soft lattice structure in perovskite materials. This work offers valuable insights into the role of polarons in nonlinear photonics, which has significant implications for advancing optoelectronics and quantum technologies.

Methods

Synthesis of $CsPbBr_3$ film

All-inorganic $CsPbBr_3$ film was fabricated by vapor-phase epitaxy methods using single-temperature zone tube furnace system. First, CsBr and $PbBr_2$ powders were mixed well with a molar ration of 1∶1, then heated to 380 °C and kept for 3 h to obtain $CsPbBr_3$ powder. Subsequently, the $CsPbBr_3$ powder (100 mg) was placed in the heating center of the tube furnace and the sapphire was placed at the downstream. The pressure was maintained at 600 Torr with Ar flow at a rate of 60 sccm as the carrier gas. The heating temperature was kept at 600 °C for 30 min for the completion of $CsPbBr_3$ film epitaxy, and then cooled down to room temperature naturally.

The ab initio molecular dynamics (AIMD) simulations

All calculations were carried out using the projector-augmented wave method in the framework of the DFT, as implemented in the Vienna ab initio Simulation Package (VASP). The generalized gradient approximation (GGA) and Perdew-Burke-Ernzerhof (PBE) exchange functional were used. The plane-wave energy cutoff was set to

500 eV, and the Γ-centered Monkhorst-Pack method with a k-mesh of 4 × 3 × 4 and 3 × 3 × 3 was employed for the Brillouin zone sampling of orthorhombic $CsPbBr_3$ and Cs_4PbBr_6, respectively. The convergence criteria of energy and force calculations were set to 10^{-6} eV/atom and 0.005 eV·Å^{-1} (1 Å = 0.1 nm), respectively. Then, these two systems were heated to 100 K, 200 K and 300 K by repeated velocity rescaling, respectively. After that, a 6 ps ab initio molecular dynamics trajectory was obtained using the microcanonical ensemble with a 1 fs time step.

Z-scan measurement

The nonlinear optical absorption was characterized by Z-scan system. The femtosecond laser source is a Ti:Sapphire regenerative amplifier system (Coherent, Astrella USP) which operating at 800 nm with 35 fs pulses at a 1 kHz repetition rate. The optical parametric amplification (TOPAS Prime, Light Conversion) system performs wavelength conversion on the output light of femtosecond laser amplifier. The femtosecond laser is then split into two beams, one used as a reference light and the other focused on the sample to excite the nonlinear optical response of the material. Two beams of light are collected by two detectors (Ophir, PD10C).

Transient absorption measurement

The femtosecond TA spectra of the perovskite film were performed using the Ultrafast System Helios TA spectrometer. The output (800 nm, 35 fs, 1 kHz) of a commercial Ti:Sapphire laser (Coherent Astrella USP) is split using a beam splitter to generate the pump and probe pulses. The pump laser is generated by an optical parametric amplification system to convert the fundamental radiation of 800 nm to the desired optical excitation wavelength. The broadband probe pulses were generated by focusing a small portion of the fundamental 800 nm laser pulses into sapphire crystals.

Results and discussion

The proposed concept of PSA_SA is illustrated in Fig. 1. In perovskite materials, when the photoexcited carriers/excitons are strongly coupled to the lattice distortion, polarizing the surrounding crystal lattice, resulting in the formation of polarons[26,36] (Fig. 1(a, b)). Such

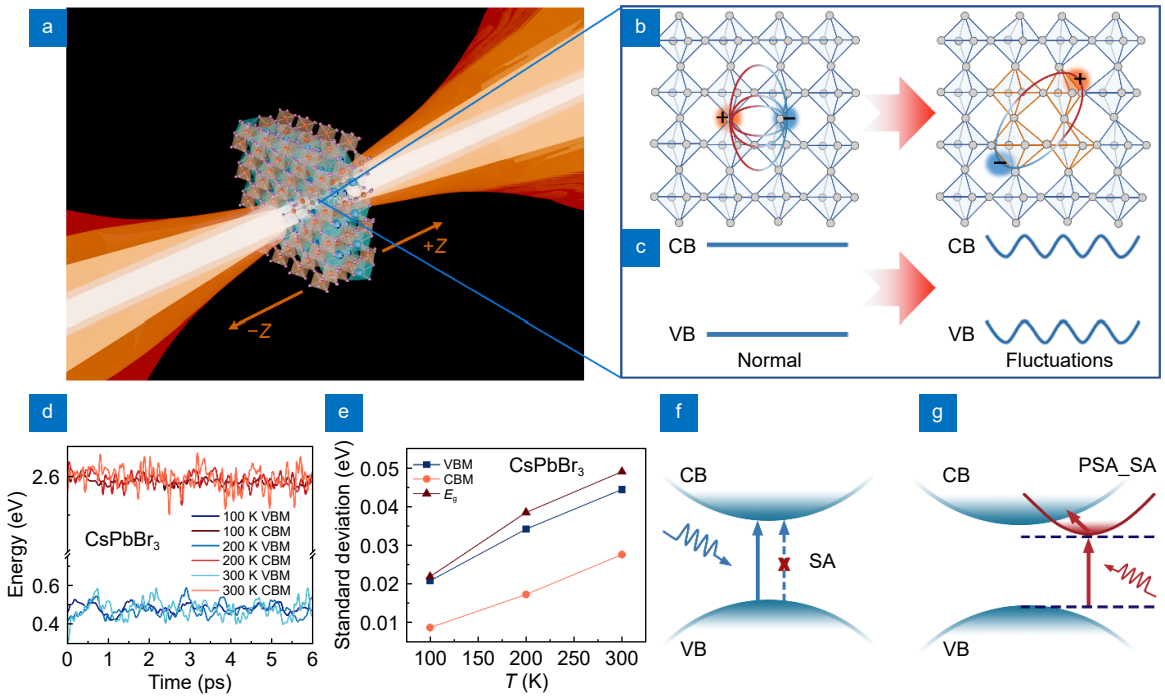

Fig. 1 | Polaronic state assisted nonlinear saturable absorption (PSA_SA) picture in LHPs. (**a**) Schematic diagram of Z-scan. (**b**) Scheme of transformation from free excitons to exciton-polaron with lattice distortion by dynamic polaronic effect. (**c**) Schematic diagram of the effect of polaron formation on the band structure of materials, which will cause band energy fluctuations. (**d**) The valence band maximum (VBM) and conduction band minimum (CBM) at different temperature are extracted according to the molecular dynamics simulation calculation results. (**e**) The standard variations of the band energy for CBM and VBM at different temperatures. (**f**) Schematic of SA caused by single photon absorption under up-bandgap excitation in conventional semiconductors. (**g**) Schematic of PSA_SA under sub-bandgap excitation. CB and VB denote conduction band and valence band respectively.

polarons have a significant effect on the energy band of a functional material[26,37], resulting in significant band energy fluctuations (Fig. 1(c)). To understand the complex interaction between excited electrons and the soft lattice of perovskite during polaron formation, DFT calculations were performed (details can be found in the *Methods* section). The representative time evolution of the band edge states during 6 ps at different temperature conditions of perovskites is obtained from ab initio molecular dynamics (AIMD) simulations (Figs. S1 and S2). It can be observed that the valence band maximum (VBM) and conduction band minimum (CBM) show strong fluctuations and increase with rising temperature (Fig. 1(d)). The bandgap variation of $CsPbBr_3$ and Cs_4PbBr_6 rise from 22 meV, 57 meV at 100 K to 49 meV and 125 meV at 300 K, respectively (Fig. 1(e) and Fig. S2). Similar to polaronic states driven anti-Stokes shift[35], the polarons involving energy fluctuation can break fundamental constraints of single photon transition SA (Fig. 1(f) and Supplementary information Section 1) and enable considerable broadband SA under sub-bandgap excitation in visible region. Normally, when the photon energy is below the band gap, SA cannot be produced in principle. However, in LHPs, exciton-phonon coupling can cause significant band energy fluctuations for polariton states, which could provide enough energy for the electrons under sub-bandgap excitation to reach the conduction band, thus producing SA in Fig. 1(g). Hence, we demonstrate another possible process for the existence of SA under sub-bandgap excitation, which is referred to as PSA_SA.

To achieve unconventional PSA_SA, a soft-lattice perovskite $CsPbBr_3$ was constructed. Figure 2(a) shows the schematic crystal structure of orthorhombic $CsPbBr_3$ and possible lattice structure distortion schemes, including rotation and tilting of the inorganic octahedral structure[38–40]. The $CsPbBr_3$ film was prepared on the sapphire substrate by vapor-phase epitaxy methods (See details in *Methods*). The scanning electron microscopy (SEM) image shows that the surface of the film is flat and smooth without any grain boundaries or cracks and energy dispersive X-ray spectroscopy (EDS) elemental mappings reveal the uniform spatial distribution of Cs, Pb and Br elements (Fig. S3). The atom force microscopy (AFM) shows that the thickness of $CsPbBr_3$ film is 184 nm and the surface roughness is less than 5 nm (Fig. S4). The X-ray diffraction (XRD) patterns in Fig. 2(b) with peaks at ~15.1°, 15.3°, 30.5° and 30.8° correspond to (002), (110), (004) and (220) planes of orthorhombic $CsPbBr_3$ (ICSD 97851), respectively. Meanwhile, no other peaks are

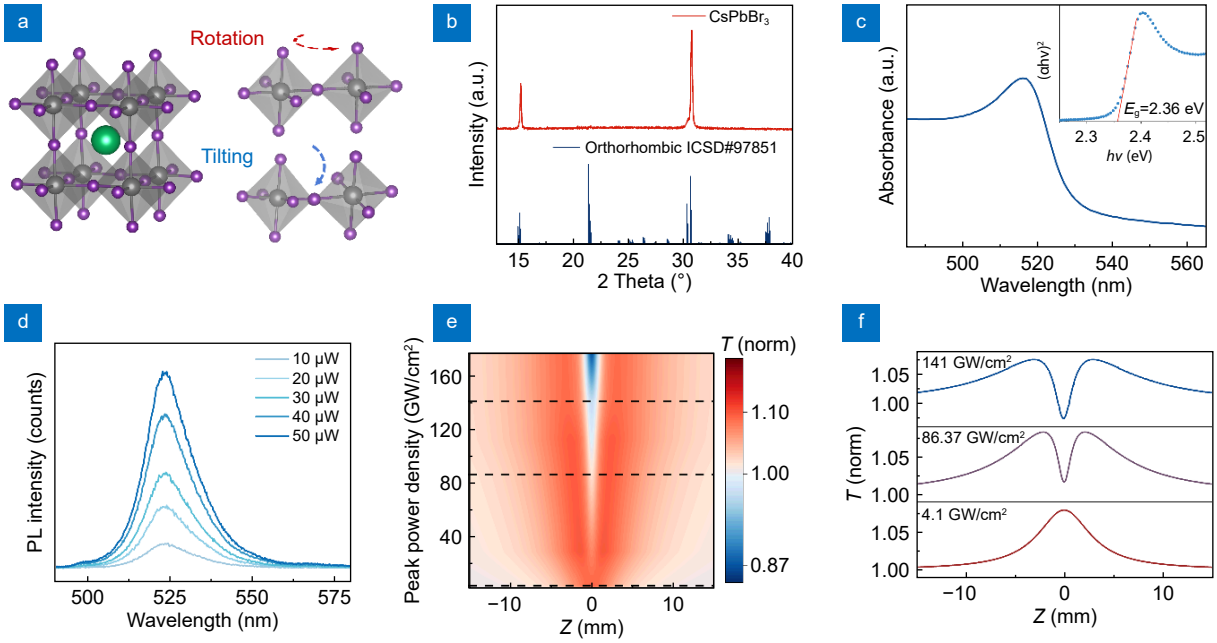

Fig. 2 | Structural, linear and nonlinear optical characterizations of $CsPbBr_3$. (**a**) Crystal structure of $CsPbBr_3$ and associated lattice distortion, where green represents Cs atoms, gray represents Pb atoms, and purple represents Br atoms. (**b**) XRD pattern of the $CsPbBr_3$ film and the standard card (ICSD-97851). (**c**) UV-vis absorption spectrum and Tauc plot of $CsPbBr_3$. (**d**) Steady PL spectra of $CsPbBr_3$ film. (**e**) The two-dimensional map of transmittance as a function of the scan distance and the excitation peak density under 530 nm laser pulse excitation and (**f**) the transmittance curves with 3 representative excitation intensities.

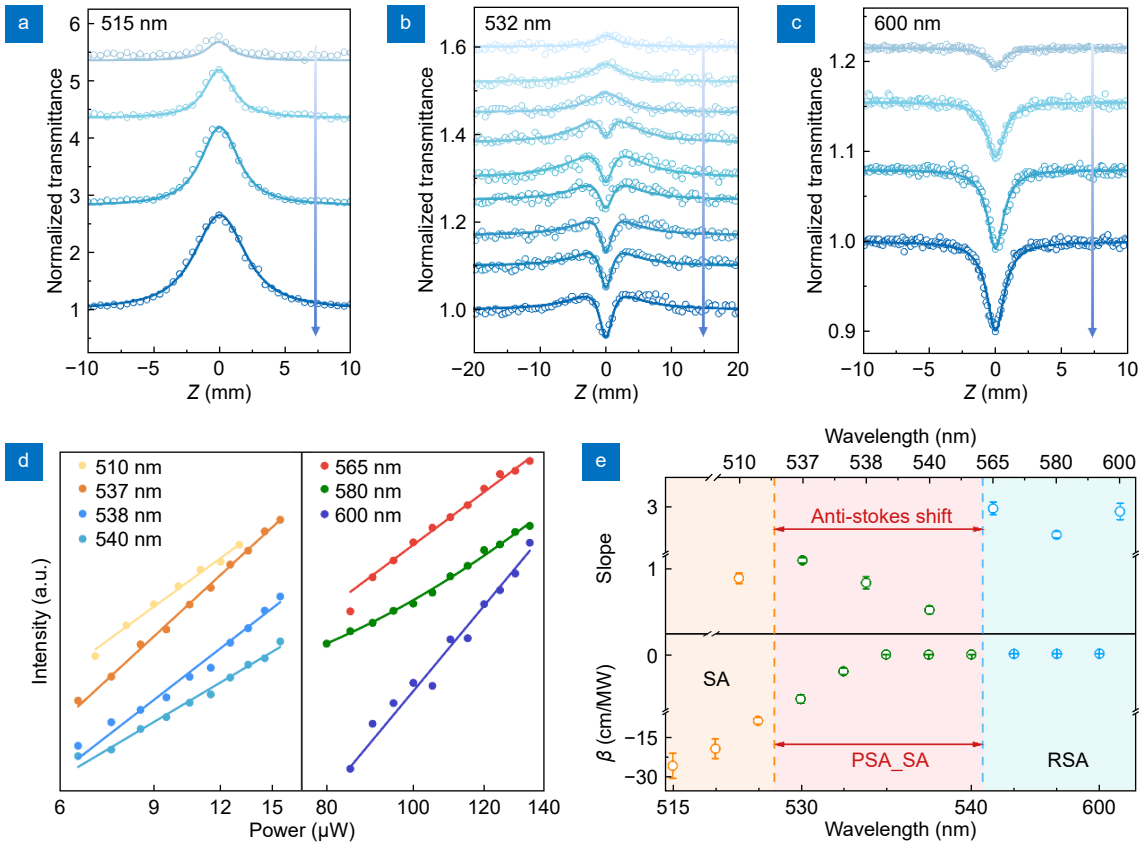

Fig. 3 | Z-scan and steady-state PL studies of polaronic state assisted nonlinear saturable absorption (PSA_SA). (**a–c**) The Z-scan results of $CsPbBr_3$ under different excitation intensity at different wavelengths. The excitation wavelengths are (a) 515 nm (pump intensity: 2.07–4.25 GW/cm^2), (b) 532 nm (pump intensity: 3.24–94.86 GW/cm^2), and (c) 600 nm (pump intensity: 48.60–215.14 GW/cm^2), respectively. From top to bottom, the light intensity increases in turn. (**d**) Power dependence of the PL intensity at different excitation wavelengths for $CsPbBr_3$. (**e**) Wavelength dependence of slope (top) and nonlinear absorption coefficient β (bottom) for $CsPbBr_3$. Error bars represent the standard error.

observed, further indicating the high crystalline purity of $CsPbBr_3$ film. As shown in Fig. 2(c), the film exhibits an absorption peak at ~516 nm, implying obvious excitonic absorption. The Tauc plot calculated from the absorption spectrum shows a bandgap of 2.36 eV (Fig. 2(c) and Supplementary information Section 2). In addition, the PL spectra show a single symmetric emission center at 524 nm (2.37 eV) with the full width of maximum (FWHM) ~16 nm (Fig. 2(d)), which is consistent with previous report[41]. We investigated the structural stability of $CsPbBr_3$ film, the XRD signals of $CsPbBr_3$ film stored in air for 4 months are almost consistent with the initial thin film (Fig. S5).

The nonlinear absorption properties of $CsPbBr_3$ film are characterized by femtosecond Z-scan technique (see Section *Methods* for details). To avoid the influence of material damage on the results, the excitation intensity was gradually increased from low to high during the Z-scan measurements. Subsequently, the Z-scan results at low laser intensity were rechecked to ensure no discrepancy with the previous measurements. The normalized excitation intensity-dependent optical transmittance under sub-bandgap excitation (2.34 eV) is presented in Fig. 2(e), which reveals that the transmittance of $CsPbBr_3$ film is distinct with increasing excitation intensity. At low light intensity, the highest transmittance appears at the focal point, which indicates SA, and when the light intensity gradually increases, the typical reverse saturable absorption (RSA) feature gradually appears with a transmittance valley near the focal point. We observe distinct SA in this perovskite under sub-bandgap excitation, as well as the characteristic nonlinear absorption conversion from SA to RSA with increasing excitation power from low to high intensity (Fig. 2(f)). Such anomalous SA does not originate from single-photon transition optical bleaching, owing to the insufficient photon energy provided by sub-bandgap excitation.

To elucidate the underlying mechanism of aforemen-

tioned anomalous SA phenomenon, the nonlinear absorption responses of $CsPbBr_3$ film were collected within the wavelength range of 515–600 nm (Fig. S6). When the excitation photon energy exceeds optical bandgap (515–525 nm), the $CsPbBr_3$ film behaves as SA (Fig. 3(a) and Fig. S6(a–c)). This behavior is attributed to the absorption change caused by electrons transition to the conduction band through single-photon absorption (schematics in Fig. 1(f)). When the excitation photon energy is slightly below the bandgap (excitation wavelength within 530–540 nm), both SA and RSA are observed in the $CsPbBr_3$ film (Fig. S6(d–h)), with a conversion from the SA to RSA as the laser intensity increases (Fig. 3(b)). It is reasonable to deduce that such a nonlinear absorption arises from the competition between two nonlinear absorption mechanism. As the excitation photon energy decreases further below the bandgap, that is, the corresponding excitation wavelength is longer than 540 nm, the SA ceases to occur, and complete RSA becomes distinctly observable (Fig. 3(c) and Fig. S6(i–k)). In principle, when the excitation photon energy is below the band gap, SA theoretically does not occur because the photon energy is insufficient to excite electrons from the valence band into the conduction band. Although two-photon absorption is energetically feasible in this case, the probability of this process occurring at low light intensity is extremely low. Although previous studies have also reported the saturable absorption phenomenon under sub-bandgap excitation and attributed it to the presence of defect states, these observations were made under conditions of relatively low incident photon energy[42,43]. Therefore, we speculate that the saturable absorption under sub-bandgap excitation may be induced by other mechanisms. Combined with the soft lattice and strong electron-phonon coupling properties of LHPs[44,45], exciton-polaron induced energy fluctuation, i.e. polaronic state, may involve in this unconventional SA process. In other words, electron-phonon coupling induced exciton-polaron facilitate the transition of low-energy electrons to the conduction band, thereby leading to the occurrence of the SA phenomenon (Fig. S6(d–e)). As the excitation photon energy gradually moves away from the band gap, the polaron energy is no longer sufficient to support the complete SA. At this time, the contribution of two-photon absorption becomes the dominant, but the SA phenomenon can still be observed, as shown in the Fig. S6(f–h). When the excitation photon energy (550–600 nm) is much smaller than the optical band gap, the $CsPbBr_3$ film exhibits a complete RSA (Fig. 3(c) and Fig. S6(i–k)). To determine whether the RSA at these wavelengths is caused by the two-photon absorption, the relationship between ln (1−T) and ln (I) is fitted. The fitting results show that k=1.1 (Fig. S7), which indicates the occurrence of a two-photon absorption dominated nonlinear RSA process[46].

To verify the PSA_SA behavior under sub-bandgap excitation, we conducted PL and ultrafast TA spectra measurements of $CsPbBr_3$ film. The PL spectra of $CsPbBr_3$ excited by photon up-conversion and down conversion processes at room temperature are shown in Fig. S8. In order to reveal the basic mechanism of PL process, the excitation power dependence of the PL intensity at each excitation wavelength is investigated. The power dependence of the PL intensity in a log-log scale for all excitation wavelengths was shown in Fig. 3(d). The measured power-dependent PL intensities are fitted with the power law[47] $I = \alpha P^S$, where P is the excitation power, α is the fitting parameter, and S is the exponent of the power law which represents the slop of the curve. The extracted values of S as a function of the corresponding excitation wavelength are further plotted in Fig. 3(e) (up panel). When the excitation wavelength $\lambda_{exc} \leq 540$ nm, both down conversion and up-conversion PL present an approximate linear or sublinear trend with the excitation density, indicating that the PL originates from exciton radiative recombination. Combined with the strong electron-phonon coupling properties, the observed linear and sublinear relationships between UCPL intensity and excitation power of $CsPbBr_3$ film suggest that UCPL follows a one-photon up-conversion process involving multi-phonon-assisted[48]. The anti-Stokes shift is defined as the energy difference between the excitation and emission peak photon energy. Thus, the anti-Stokes shift corresponding to phonon-assisted UCPL in $CsPbBr_3$ is about 70 meV (Fig. S9(a)). When the excitation wavelength $\lambda_{exc} \geq 565$ nm, the slope of UCPL is almost three times correlated with the excitation density dependence. This may be due to nonlinear optical effects caused by multiple-photon absorption or Auger recombination[49,50], because these mechanisms typically display a superlinear (quadratic or more) excitation power dependence.

In order to clarify the SA phenomenon below the bandgap excitation more directly, we calculate the nonlinear absorption coefficients of $CsPbBr_3$ at different excitation wavelengths (Supplementary information Section 3), as shown in Fig. 3(e) (down panel). It can be

observed that the nonlinear absorption response of $CsPbBr_3$ is strongest when the excitation photon energy resonates with the absorption peak. As the excitation photon energy moves away from the resonance region, the nonlinear absorption response gradually weakens, and the nonlinear absorption coefficient transitions from negative to positive. This indicates that as the excitation photon energy decreases, SA gradually shifts to RSA. According to the nonlinear absorption characteristics and the nonlinear absorption coefficient, the excitation wavelengths are divided into three regions: the SA region caused by pure single photon absorption when the excitation photon energy exceeds the band gap ($\lambda_{exc} \leq 525$ nm); the RSA region which caused by two-photon absorption when the excitation photon energy is significantly lower than the bandgap ($\lambda_{exc} \geq 550$ nm); and the region in which SA and RSA coexist when the excitation photon energy marginally less than the bandgap (530 nm $\leq \lambda_{exc} \leq$ 540 nm). The energy shift is defined as the difference between the excitation photon energy corresponding to the SA effect still existing in $CsPbBr_3$ under sub-bandgap excitation and the optical band gap, which is about 60 meV (Fig. S9(b)). The nonlinear optical response of $CsPbBr_3$ film depending on excitation photon energy shows high consistency with corresponding PL results. The single photon fluorescence region corresponds to the SA region; the region where SA and RSA coexist is consistent with the region of one-photon upconversion involving phonon-assisted; and the multiphoton fluorescence region corresponds to the RSA region. Notably, the phonon-involved anti-Stokes shift invariably overlaps with the sub-bandgap excitation SA occurrence band region, providing strong evidence for excitation-polarons-assisted SA. In addition, we also observe a similar phenomenon in another perovskite (Cs_4PbBr_6). The PL spectra and *Z*-scan results of Cs_4PbBr_6 at different excitation wavelengths are shown in Fig. S10 and Fig. S11. The power dependence of the PL intensity for all excitation wavelengths and the extracted values of *S* as a function of the corresponding excitation wavelength are shown in Fig. S12(a) and S12(b) (up panel). Since the emission center of Cs_4PbBr_6 is at 517 nm, the phono-assisted anti-Stokes shift obtained from the experimental results is about 102 meV. According to the absorption spectrum, it can be observed that Cs_4PbBr_6 has an absorption edge at 517 nm (Fig. S13(a)) and the optical band gap calculated by Tauc method is about 2.32 eV (Fig. S12(b)). Combined with the *Z*-scan results (Fig. S12(b) (down panel)), it is obtained that the energy shift is about 70 meV. The energy shift of Cs_4PbBr_6 is larger than that of $CsPbBr_3$, which is due to the fact that Cs_4PbBr_6 with decoupled octahedra is susceptible to perturbation by photoexcitation, while $CsPbBr_3$ has a rather rigid inorganic framework[51]. In order to prove this speculation, we calculate the Young's modulus of two perovskites by DFT (see details in Supplementary information Section 4). Different models are used to calculate the Young's modulus for each system (Table S1). The results show that the Young's modulus of Cs_4PbBr_6 (16.52 Gpa) is smaller than that of orthorhombic $CsPbBr_3$ (17.98 Gpa). Apart from the mean value of Young's modulus, the calculated anisotropy of Young's modulus (Table S2 and Fig. S14) further demonstrate that Cs_4PbBr_6 exhibits a "softer" lattice feature compared with $CsPbBr_3$. The bandgap variation of Cs_4PbBr_6 increases from 57 meV (100 K) to 125 meV (300 K), indicating that the energy band fluctuation of LHPs with softer crystal lattice is more significant. These calculation results demonstrate that Cs_4PbBr_6 with "softer" lattice facilitates stronger electron-phonon coupling during light-matter interaction. In addition, these results also show that the optical nonlinearity can be regulated by adjusting the lattice structure.

In order to further reveal the mechanism of PSA_SA in $CsPbBr_3$ film under sub-bandgap excitation, we perform systematic ultrafast TA measurements (see *Methods* for details) of $CsPbBr_3$. Figure 4(a–c) show the pseudo-color plot of TA difference (ΔA) as a function of probe light wavelength and delay time at different excitation wavelengths. As shown in Fig. 4(d), when photoexcitation energy is larger than the band gap (515 nm), the TA profile displays a negative peak at the exciton resonance ($\Delta A < 0$) and two positive peaks at either side ($\Delta A > 0$), in which the negative signal represents photobleaching and the positive signal represents photo-induced absorption. These features are a synthesis of the state filling of the exciton band and the effects of exciton band broadening and shifting caused by multibody interactions in the presence of excitons and carriers[35,52]. When the excitation photon energy (530 nm) is slightly less than the band gap, the TA spectra show a slight blueshift (Fig. 4(b) and 4(e)). After this slight blueshift, the transient spectral characteristic for the excitation below the gap is similar to that for the excitation above the gap. When the photon energy (600 nm) is much smaller than the optical band gap, the TA spectra show an

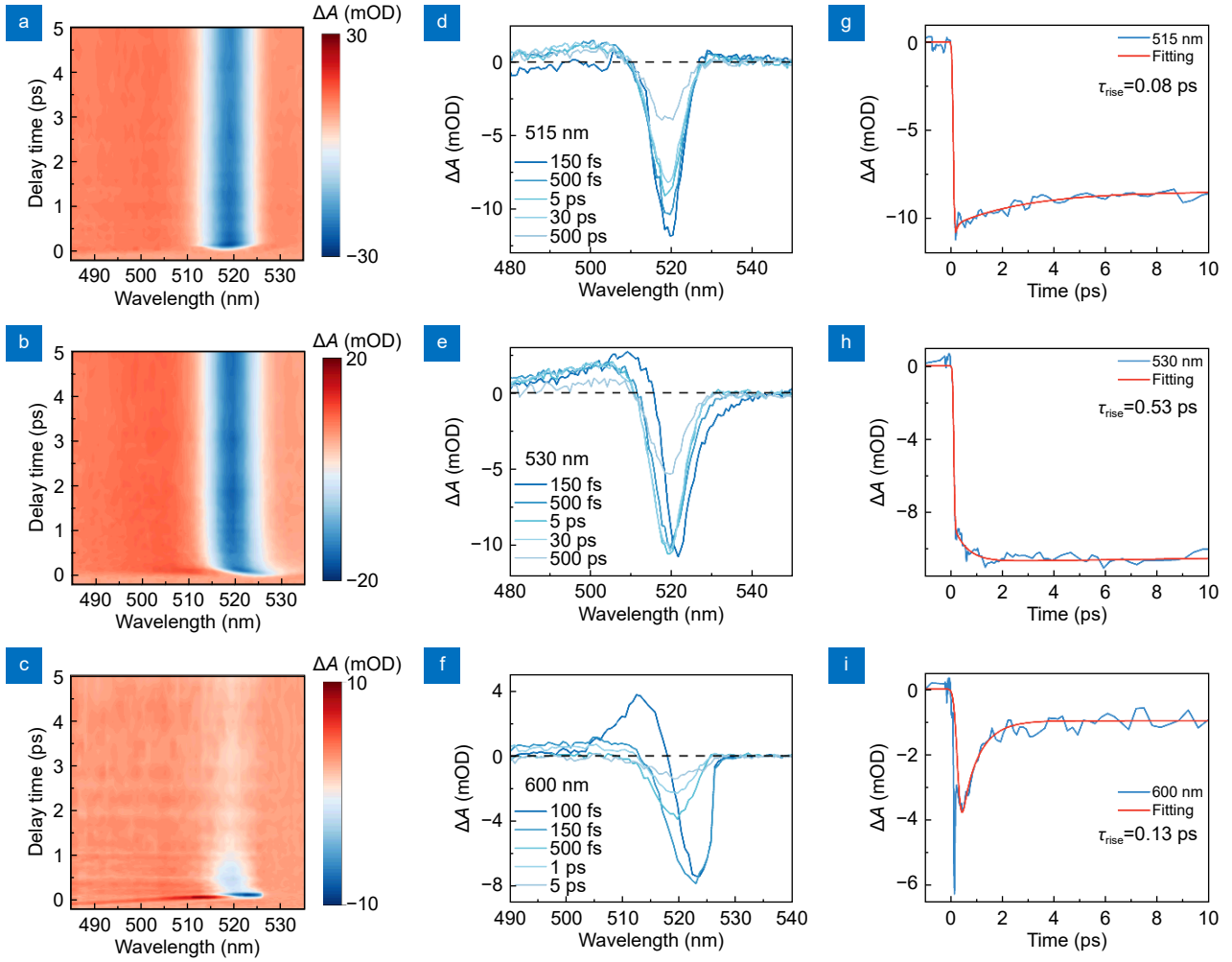

Fig. 4 | TA measurements confirming polaronic state assisted nonlinear saturable absorption (PSA_SA). (**a–c**) Representative pseudocolor TA spectrums at (a) 515 nm, (b) 530 nm and (c) 600 nm excitations, respectively. (**d–f**) Time-dependent photo-induced changes in absorption (Δ*A*) which is pumped by (d) 515 nm , (e) 530 nm and (f) 600 nm , respectively. (**g–i**) Exciton band bleach dynamics monitored at 519 nm for (g) 515 nm , (h) 530 nm, and (i) 600 nm excitations, respectively.

instantaneous giant response at time zero corresponding to the blueshift of excitation (Fig. 4(c) and 4(f)). This is due to the optical Stark effect caused by the hybridization of the equilibrium and Floquet states[35,53]. In addition, the transient dynamics monitored at the exciton band (~519 nm) under different excitation wavelengths are extracted (Fig. 4(g–i) and Fig. S15). The rise time for the exciton band bleaching under 515 nm excitation is around 0.08 ps (Fig. 4(g)), which corresponds to the time required for the excitations to scatter to the band edge by optical phonons[35,54]. For 530 nm excitation, the rising of exciton band bleach is relatively slower with a time constant of 0.53 ps (Fig. 4(h)). When the excitation photon energy is much less than the band gap, two-photon absorption will dominate due to the larger pump energy. After removing the strong nonlinear response by optical Stark effect, the rise time of exciton band bleach is around 0.13 ps (Fig. 4(i)). The corresponding relationship between the rise time of exciton band bleaching and excitation wavelength is shown in Fig. S16. When the excitation photon energy is larger than the optical band gap (515–525 nm), the average rise time of this band is almost 0.08 ps; when the photon energy is slightly less than the band gap (530–540 nm), the average rise time is around 0.60 ps; when the photon energy is much less than the band gap (550–600 nm), the average rise time is around 0.15 ps. When the excitation photon energy is slightly less than the band gap, the rise time of exciton band bleaching is slower, indicating the occurrence of strong electron-phonon interaction that lead to the emergence of excitation polarons, while simultaneously ruling out the presence of defect states[35,37,55]. The results

of TA also consistent with PL and Z-scan results, further confirming that the SA under sub-bandgap excitation is assisted by exciton-polarons induced polarons state.

Conclusions

In conclusion, we have investigated the nonlinear absorption properties of LHPs at room temperature and revealed the PSA_SA behavior under sub-bandgap excitation. The DFT calculations show that the strong fluctuations of band energy caused by the rapid lattice deformation and formation of polarons, which leads to the substantial energy shift. The polarons involving energy fluctuation assistance can break the basic restriction of single-photon transition and provide sufficient energy for single-photon absorption under sub-bandgap excitation. We have further identified that the perovskite with "softer" lattice exhibits greater band energy fluctuation and facilitates stronger carrier/excitons-phonon coupling induced polarons. Our findings reveal that modulating the lattice properties of LHPs may be a way of adjusting the polaron states to broaden nonlinear absorption applications.

References

1. Boyd RW, Masters BR. Nonlinear optics, third edition. *J Biomed Opt* **14**, 029902 (2009).
2. Guo QB, Qi XZ, Zhang LS et al. Ultrathin quantum light source with van der Waals $NbOCl_2$ crystal. *Nature* **613**, 53–59 (2023).
3. Chang DE, Vuletić V, Lukin MD. Quantum nonlinear optics—photon by photon. *Nat Photonics* **8**, 685–694 (2014).
4. Guo QS, Sekine R, Ledezma L et al. Femtojoule femtosecond all-optical switching in lithium niobate nanophotonics. *Nat Photonics* **16**, 625–631 (2022).
5. Guo QS, Gutierrez BK, Sekine R et al. Ultrafast mode-locked laser in nanophotonic lithium niobate. *Science* **382**, 708–713 (2023).
6. Hu YW, Yu MJ, Zhu D et al. On-chip electro-optic frequency shifters and beam splitters. *Nature* **599**, 587–593 (2021).
7. Cui CH, Zhang L, Fan LR. In situ control of effective Kerr nonlinearity with Pockels integrated photonics. *Nat Phys* **18**, 497–501 (2022).
8. Chen Z, Li JF, Li TZ et al. A CRISPR/Cas12a-empowered surface plasmon resonance platform for rapid and specific diagnosis of the Omicron variant of SARS-CoV-2. *Natl Sci Rev* **9**, nwac104 (2022).
9. Chen Z, Huang H, Deng J et al. Light - guided genetic scissors based on phosphorene quantum dot. *Laser Photonics Rev* **18**, 2400777 (2024).
10. Chen Z, Meng CL, Wang XL et al. Ultrasensitive DNA origami plasmon sensor for accurate detection in circulating tumor DNAs. *Laser Photonics Rev* **18**, 2400035 (2024).
11. Bao QL, Zhang H, Wang Y et al. Atomic-layer graphene as a saturable absorber for ultrafast pulsed lasers. *Adv Funct Mater* **19**, 3077–3083 (2009).
12. Wang KP, Zhang XY, Kislyakov IM et al. Bacterially synthesized tellurium nanostructures for broadband ultrafast nonlinear optical applications. *Nat Commun* **10**, 3985 (2019).
13. Dong YC, Chertopalov S, Maleski K et al. Saturable absorption in 2D Ti_3C_2 MXene thin films for passive photonic diodes. *Adv Mater* **30**, 1705714 (2018).
14. Zhou L, Kang JL, Dong YL et al. Solvent-stabilized few-layer violet phosphorus and its ultrafast nonlinear optics. *Nano Res* **16**, 5843–5849 (2023).
15. Wang YW, Huang GH, Mu HR et al. Ultrafast recovery time and broadband saturable absorption properties of black phosphorus suspension. *Appl Phys Lett* **107**, 091905 (2015).
16. Jiang T, Huang D, Cheng JL et al. Gate-tunable third-order nonlinear optical response of massless Dirac fermions in graphene. *Nat Photonics* **12**, 430–436 (2018).
17. Hong H, Wu CC, Zhao ZX et al. Giant enhancement of optical nonlinearity in two-dimensional materials by multiphoton-excitation resonance energy transfer from quantum dots. *Nat Photonics* **15**, 510–515 (2021).
18. Wang YD, Wang YW, Lan CY et al. Interfacial charge transfer for enhancing nonlinear saturable absorption in WS_2/graphene heterostructure. *Adv Sci* **11**, 2306096 (2024).
19. Dirnberger F, Quan JM, Bushati R et al. Magneto-optics in a van der Waals magnet tuned by self-hybridized polaritons. *Nature* **620**, 533–537 (2023).
20. Tang YX, Zhang YB, Liu QR et al. Interacting plexcitons for designed ultrafast optical nonlinearity in a monolayer semiconductor. *Light Sci Appl* **11**, 94 (2022).
21. Gu LX, Zhang LF, Ni RH et al. Giant optical nonlinearity of Fermi polarons in atomically thin semiconductors. *Nat Photonics* **18**, 816–822 (2024).
22. Puppin M, Polishchuk S, Colonna N et al. Evidence of large polarons in photoemission band mapping of the perovskite semiconductor $CsPbBr_3$. *Phys Rev Lett* **124**, 206402 (2020).
23. Qian Q, Wan Z, Takenaka H et al. Photocarrier-induced persistent structural polarization in soft-lattice lead halide perovskites. *Nat Nanotechnol* **18**, 357–364 (2023).
24. Yaffe O, Guo YS, Tan LZ et al. Local polar fluctuations in lead halide perovskite crystals. *Phys Rev Lett* **118**, 136001 (2017).
25. Tao WJ, Zhang C, Zhou QH et al. Momentarily trapped exciton polaron in two-dimensional lead halide perovskites. *Nat Commun* **12**, 1400 (2021).
26. Biswas S, Zhao RY, Alowa F et al. Exciton polaron formation and hot-carrier relaxation in rigid Dion–Jacobson-type two-dimensional perovskites. *Nat Mater* **23**, 937–943 (2024).
27. Guzelturk B, Winkler T, Van de Goor TWJ et al. Visualization of dynamic polaronic strain fields in hybrid lead halide perovskites. *Nat Mater* **20**, 618–623 (2021).
28. Luo TC, Ilyas B, von Hoegen A et al. Time-of-flight detection of terahertz phonon-polariton. *Nat Commun* **15**, 2276 (2024).
29. Kim D, Jung HJ, Park IJ et al. Efficient, stable silicon tandem cells enabled by anion-engineered wide-bandgap perovskites. *Science* **368**, 155–160 (2020).
30. Ren XX, Wang JF, Lin Y et al. Mobile iodides capture for highly photolysis- and reverse-bias-stable perovskite solar cells. *Nat Mater* **23**, 810–817 (2024).
31. Zhu HM, Fu YP, Meng F et al. Lead halide perovskite nanowire lasers with low lasing thresholds and high quality factors. *Nat Mater* **14**, 636–642 (2015).
32. Chen QS, Wu J, Ou XY et al. All-inorganic perovskite nanocrys-

tal scintillators. *Nature* **561**, 88–93 (2018).
33. Anantharaman SB, Lynch J, Stevens CE et al. Dynamics of self-hybridized exciton–polaritons in 2D halide perovskites. *Light Sci Appl* **13**, 1 (2024).
34. Gong YY, Yue S, Liang Y et al. Boosting exciton mobility approaching Mott-Ioffe-Regel limit in Ruddlesden−Popper perovskites by anchoring the organic cation. *Nat Commun* **15**, 1893 (2024).
35. Wu B, Wang AC, Fu J et al. Uncovering the mechanisms of efficient upconversion in two-dimensional perovskites with anti-Stokes shift up to 220 meV. *Sci Adv* **9**, eadi9347 (2023).
36. Dai ZB, Lian C, Lafuente-Bartolome J et al. Theory of excitonic polarons: from models to first-principles calculations. *Phys Rev B* **109**, 045202 (2024).
37. Miyata K, Meggiolaro D, Trinh MT et al. Large polarons in lead halide perovskites. *Sci Adv* **3**, e1701217 (2017).
38. Li W, Vasenko AS, Tang JF et al. Anharmonicity extends carrier lifetimes in lead halide perovskites at elevated temperatures. *J Phys Chem Lett* **10**, 6219–6226 (2019).
39. Shao Y, Gao W, Yan HJ et al. Unlocking surface octahedral tilt in two-dimensional Ruddlesden-Popper perovskites. *Nat Commun* **13**, 138 (2022).
40. Gu T, Scarbrough T, Yang YR et al. Cooperative couplings between octahedral rotations and ferroelectricity in perovskites and related materials. *Phys Rev Lett* **120**, 197602 (2018).
41. Zhong YG, Liao K, Du WN et al. Large-scale thin $CsPbBr_3$ single-crystal film grown on sapphire *via* chemical vapor deposition: toward laser array application. *ACS Nano* **14**, 15605–15615 (2020).
42. Mushtaq A, Kushavah D, Ghosh S et al. Nonlinear optical properties of benzylamine lead(II) bromide perovskite microdisks in femtosecond regime. *Appl Phys Lett* **114**, 051902 (2019).
43. Zhang XY, Zhang SF, Xie YF et al. Tailoring the nonlinear optical performance of two-dimensional MoS_2 nanofilms *via* defect engineering. *Nanoscale* **10**, 17924–17932 (2018).
44. Yamada Y, Kanemitsu Y. Electron-phonon interactions in halide perovskites. *NPG Asia Mater* **14**, 48 (2022).
45. Wright AD, Verdi C, Milot RL et al. Electron–phonon coupling in hybrid lead halide perovskites. *Nat Commun* **7**, 11755 (2016).
46. Wang YD, Wang YW, Chen KQ et al. Niobium carbide MXenes with broad-band nonlinear optical response and ultrafast carrier dynamics. *ACS Nano* **14**, 10492–10502 (2020).
47. Mushtaq A, Yang XD, Gao J. Unveiling room temperature upconversion photoluminescence in monolayer WSe_2. *Opt Express* **30**, 45212–45220 (2022).
48. Roy S, Yang XD, Gao J. Uniaxial strain tuning of upconversion photoluminescence in monolayer WSe_2. *Adv Photonics Res* **5**, 2300220 (2024).
49. Akizuki N, Aota S, Mouri S et al. Efficient near-infrared up-conversion photoluminescence in carbon nanotubes. *Nat Commun* **6**, 8920 (2015).
50. Ma YZ, Valkunas L, Dexheimer SL et al. Femtosecond spectroscopy of optical excitations in single-walled carbon nanotubes: evidence for exciton-exciton annihilation. *Phys Rev Lett* **94**, 157402 (2005).
51. Wang LL, Liu H, Zhang YH et al. Photoluminescence origin of zero-dimensional Cs_4PbBr_6 perovskite. *ACS Energy Lett* **5**, 87–99 (2020).
52. Thouin F, Valverde-Chávez DA, Quarti C et al. Phonon coherences reveal the polaronic character of excitons in two-dimensional lead halide perovskites. *Nat Mater* **18**, 349–356 (2019).
53. Giovanni D, Chong WK, Dewi HA et al. Tunable room-temperature spin-selective optical Stark effect in solution-processed layered halide perovskites. *Sci Adv* **2**, e1600477 (2016).
54. Wu XX, Trinh MT, Zhu XY. Excitonic many-body interactions in two-dimensional lead iodide perovskite quantum wells. *J Phys Chem C* **119**, 14714–14721 (2015).
55. deQuilettes DW, Frohna K, Emin D et al. Charge-carrier recombination in halide perovskites. *Chem Rev* **119**, 11007–11019 (2019).

Acknowledgements

This research was supported by the National Natural Science Foundation of China (Grant Nos. 62275275, 11904239, 62422506, 12474383, 52273202), National Key R&D Program of China (2022YFA1604200), Natural Science Foundation of Hunan Province (Grant Nos. 2021JJ40709, 2022JJ20080, 2024JJ6481) and Postgraduate Innovative Project of Central South University (Grant No. CX20230246). This work was also supported in part by the High-Performance Computing Center of Central South University and Open Sharing Found for the Large-scale Instruments and Equipment of Central South University. We also acknowledge resources from the Hefei Advanced Computing Center.

Author contributions

Y. W. Wang and J. He conducted and supervised the project. L. Zhou fabricated the perovskite film, conducted a series of data collection and analysis. Y. D. Wang and C. Tong carried out the density functional theory calculations. J. Kang, X. Li, Q. Long and X. Zhong helped with the optical tests. L. Zhou and Z. Chen carried out the photoluminescence measurements. K. Chen synthesized the zero-dimensional perovskite sample. Z.-L. Deng, Z. Zhang, C. Shu, Y. Yuan, X. Ni, S. Xiao and X. Li helped with meaningful discussion and polishing the manuscript. All authors contributed to the redaction of the manuscript and agreed with the final version of the manuscript.

Competing interests

Xiangping Li serves as an Editor for the Journal, and no other author has reported any competing interests.

Supplementary information

Supplementary information for this paper is available at https://doi.org/10.29026/oea.2025.240312

Scan for Article PDF